# Earthquakes Felt in the Juan Fernandez Islands: Where Are They Coming from?

Sebastián Carrasco[*1,2], Sergio Ruiz[3], and Miguel Sáez[3]

## Abstract

The Juan Fernandez Islands (JFI) are located in the Pacific Ocean 675 km west of the Chilean coast. This archipelago has historically been affected by large tsunamis. Robinson Crusoe Island (RCI), the main island of the JFI, was first inhabited in 1749. Since then, several tsunamis have destroyed RCI port structures and sometimes caused deaths. Ground shaking perceived by the inhabitants has preceded some tsunami arrivals. Seismological instrumentation was temporarily deployed on RCI in 1999, and a permanent station has been operating since 2014. Here, we use these data to characterize the seismic waves that arrive at the JFI and to determine whether shaking perception could be used as a tsunami early warning system. We compute peak ground accelerations (PGAs) from *P*, *S*, and *T* waves generated by Peruvian and Chilean earthquakes and find that the largest ground shakings are mostly related to *T*-wave arrivals, which correlate with macroseismic modified Mercalli intensities lower than III. From the analysis of PGAs and macroseismic intensities, we conclude that shaking perception can be associated with large megathrust earthquakes, subduction events generated in the deep zone of seismogenic contact, and local seismicity. Unfortunately, potential tsunami earthquakes that occur on the Chilean coast will not be felt on RCI. Consequently, ground shaking in the JFI would not be a good proxy for tsunami warning, and a robust tsunami early warning system is necessary for RCI.
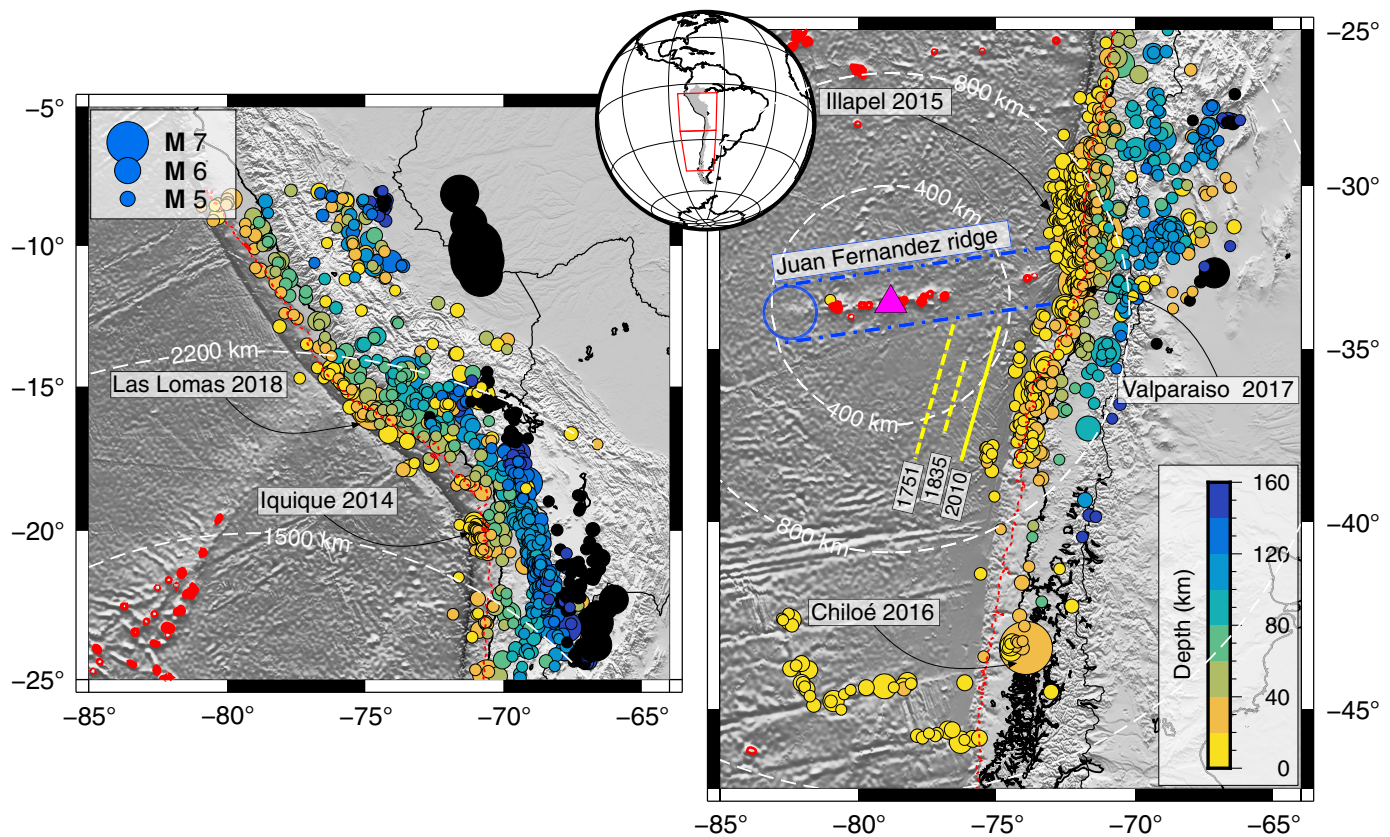
## Introduction

The Juan Fernandez Islands (JFI) are intraplate volcanic islands located at latitude 33° S, longitude 79° W, ~675 km west of central Chile. They rise from the Juan Fernandez ridge (JFR), a discontinuous array of volcanic centers aligned approximately east–west, whose origin has been attributed to an active hot spot located west of Robinson Crusoe Island (RCI), as shown in Figure 1 (Von Huene *et al.*, 1997). The JFI have been devastated by tsunamis produced by earthquakes generated along the Chilean margin. Written reports exist since 1749, when the Spanish crown ordered the building of the Saint Barbara Fortress and the populating of RCI. The first reports of earthquake-related activity dates back to 1751, when the tsunami generated by the 1751 Concepción megathrust earthquake reached the coast of RCI, causing 36 deaths and destroying houses, warehouses, the church, and the governor's house (Udías *et al.*, 2012; based on "Documents of the Archivo de Indias," located in Spain). The governor of JFI, Thomas Sutcliffe, reported the effects of the 20 February 1835 south-central Chile megathrust earthquake. This earthquake generated a large tsunami that reached the RCI, destroyed the harbor and triggered the eruption of a submarine volcano located near JFI, which generated a slight shaking felt on RCI (Sutcliffe, 1839; Montessus de Ballore, 1911/1916). During the twentieth century, three earthquakes

were reported to occur in the area surrounding the RCI in the 1980s (Wysession *et al.*, 1991), and two of them were confirmedly felt by RCI inhabitants (E. Okal, personal comm., 2019). Between October and December 1998, earthquake shaking was reported by inhabitants of RCI, where macroseismic intensities (MsIs) reached III–IV modified Mercalli intensity (MMI). A quick deployment of seismological stations in March 1999 provided some information about local seismicity, and the most important outcome was the identification of *S-P* times even shorter than 3 s (Chilean National Emergency Office [ONEMI], 1999; see Fig. S1, available in the supplemental material to this article). During the 27 February 2010 Maule $M_w$ 8.8 Chile megathrust earthquake (Ruiz and Madariaga, 2018), RCI inhabitants felt ground shaking before a tsunami arrived at the island, which finally destroyed most of the coastline buildings and left 18 fatalities and much damage (Fritz *et al.*, 2011). The 2015 Illapel $M_w$ 8.3 earthquake, located due east of

**Figure 1.** Seismological context of the Juan Fernandez Islands (JFI). Yellow solid line represents length of rupture area of the 2010 $M_w$ 8.8 Maule earthquake. Dashed yellow line is the inferred rupture length of 1751 and 1835 earthquakes. Robinson Crusoe Island (RCI), one of the main islands of JFI and where VA04 station is installed, is illustrated by the magenta triangle. Solid circles correspond to regional seismicity studied in this work scaled by magnitude and filled according to hypocenter depth. Juan Fernandez ridge is delimited by the blue dashed-dotted lines, and its hot spot is noted by the open blue circle. Some large earthquakes are also noted. Isoepicentral distances contours from VA04 station at 400, 800, 1500, and 2200 km are drawn with white dashed lines. Topographic features in the Nazca plate where bathymetry reaches 1200 m below sea level are illustrated by red polygons. The 1200 m depth level in the continental slope is denoted by the red dashed line. (Inset) Global map with the specified studied area. The color version of this figure is available only in the electronic edition.

the JFI, was also felt by RCI inhabitants. Finally, ground shaking was reported by RCI inhabitants during the $M_w$ 7.1 Las Lomas earthquake on 17 January 2018, which occurred more than 2000 km from the island and did not cause any fatalities or damage in the JFI. The rupture lengths of the three large earthquakes affecting RCI are illustrated in Figure 1, along with regional seismicity with $M \geq 4.5$ located by the National Earthquake Information Center (NEIC) from June 2014 through January 2019.

A multiparametric seismological station of the National Seismological Center of University of Chile (CSN) has been running since 2014 on RCI. The strong-motion instrument and the broadband seismometer have recorded several large-magnitude earthquakes from the Chile–Peru trench such as the 2015 $M_w$ 8.3 Illapel, 2016 $M_w$ 7.6 Chiloé, and 2018 $M_w$ 7.1 Las Lomas earthquakes and more than 180 earthquakes with $M_w \geq 5.5$ since its installation (see Fig. 1).

Currently, the perception of earthquakes by RCI inhabitants has been related to large tsunamigenic megathrust earthquakes. Here, we use these data from the CSN station to determine where the earthquakes felt in RCI originate. To achieve this goal, we consider 1803 earthquakes with magnitudes higher than 4.5 occurring along the Peruvian–Chilean margin and recorded on RCI to characterize the peak ground acceleration (PGA) generated by different seismic waves. Then we relate the PGA of the $T$ phase to the MsI and compare this behavior with the $T$-phase energy flux (TPEF). We observe that

the different kinds of earthquakes correlate in different forms with the PGA and MsI. Finally, we discuss whether this relation between PGA and MsI could be used as a potential tsunami warning.

## Data and Methods
### Seismological instruments

The high-frequency arrival of $P$ and $S$ waves and especially $T$ phases are well recorded in seismological stations located on islands (Okal, 2011). Here, we use data from the VA04

seismological station on RCI (Fig. 1) to analyze these high-frequency waves (see Data and Resources). This station is maintained and operated by CSN and is located inside Juan Fernández National Park at 117 m vertical elevation and ~220 m from the island coastline at a site characterized by partially eroded volcanic sequences (Leyton et al., 2018). The station is equipped with a broadband Trillium 120 s period sensor and a strong-motion CMG-5T sensor with a 2.4g clip level, both continuously recording with a sample rate of 100 Hz. The operation time range started in June 2014, and only some small data gaps have occurred because of malfunction of the station (Fig. S1 shows the available data). According to this information, we consider earthquakes occurring from 6 June 2014 until 31 January 2019 (see Data and Resources). The earthquake catalog was retrieved from the NEIC-U.S. Geological Survey for an area delimited by 8°–58° S and 99°–64° W; our preliminary catalog contains 2137 events with magnitudes **M** ≥ 4.5.

## Main seismic sequences recorded in the JFI

The VA04 station on RCI has been able to record seismic waves from earthquakes related to different seismic sequences occurring along the Peruvian–Chilean coast. These seismic sequences are mainly related to large subduction interface earthquakes (**M** > 7), which provide events with a wide range of magnitudes at different locations along the subduction margin (Fig. 1). Among these sequences, we can highlight the aftershock sequence of the 2014 $M_w$ 8.2 Iquique earthquake, which was located mainly in the up-dip region of the interface (Cesca et al., 2016; León-Ríos et al., 2016). In addition, the station recorded the whole Illapel sequence of 2015, including its mainshock, which has been proposed to have slipped along almost the entire thrust interface, and its aftershocks, which occurred mainly along the plate contact at depths ranging from shallow to ~50 km (e.g., Li et al., 2016; Melgar et al., 2016; Ruiz et al., 2016; Tilmann et al., 2016; Carrasco et al., 2019, and references therein). The 2016 $M_w$ 7.6 Chiloé earthquake occurred at ~35 km depth and was also recorded on RCI, but it had only one aftershock with a magnitude larger than 5 (Ruiz, Moreno, et al., 2017; Lange et al., 2018). On the other hand, the 2017 $M_w$ 6.9 Valparaiso sequence included significant events with **M** ≥ 5.5 (e.g., Ruiz, Aden-Antoniow, et al., 2017). Recently, the 2018 $M_w$ 7.1 Las Lomas earthquake occurred at greater depth along the thrust interface (~40 km) and was also recorded with all its surrounding events distributed prior to and after the mainshock.

## MsIs: instrumental and perception

The perception of earthquake shaking can be described through instrumental MsI, which is based on observational features during and after shaking. Instrumental MsI can be defined for peak ground motion parameters such as peak ground velocity or PGA. Here, we consider the PGA amplitudes to obtain the MMI using ground motion to intensity conversion equations (GMICEs; Cua et al., 2010). In this way,

a summary of several GMICEs shows that lower intensities can be reached from a wide range of PGAs. Because low shaking perception (MMI < V) is usually related to PGA values, PGA amplitudes recorded by strong-motion sensors provide a good estimate of MsI. Here, we estimate the MsI felt on RCI according to the equation proposed by Wald et al. (1999):

$$\text{MMI} = 2.20 \log(\text{PGA}) + 1.0, \tag{1}$$

with PGA in cm/s/s.

The MsI is computed for each P and S waves and T phase. For this calculation, we computed the P- and S-wave theoretical arrival times with a Python implementation of Java TauP toolkit by Crotwell et al. (1999) through ObsPy package (Beyreuther et al., 2010), assuming a 1D spherically symmetric Earth model given by ak135 model (Kennett et al., 1995). However, the computation of T-phase arrival times cannot be obtained directly from TauP toolkit as P and S waves do because T phase correspond to a combination of a P (or S) wave traveling through solid Earth and a T wave traveling through water. The latter is originated when the corresponding P (or S) wave reaches the interface between water (usually ocean) and crust at depths where the sound fixing and ranging (SOFAR) channel is located (between 700 and 1300 m). Thus, to estimate the T-phase arrival times, we divided the procedure in two stages. First, we computed the travel time $t_{Ph}$ of a P wave from the hypocenter to the SOFAR channel interface along the continental slope using the TauP toolkit. Second, we computed the travel time $t_{TW}$ of a T-wave traveling at 1.5 km/s from the SOFAR channel interface to VA04 station and considering the epicentral distance between these two points. The T-phase arrival time $t_{TP}$ is finally estimated as the simple summation of $t_{Ph}$ and $t_{TW}$. We estimated the location of the SOFAR channel interface as the 1200 m depth level along the Peru–Chile continental slope obtained from the ETOPO1 grid (Amante and Eakins, 2009) as shown in Figure 1. From these theoretical arrival times, we selected a window of data for each type of wave. For P and S waves, the data window starts 30 s before respective arrival time and spans 180 s after it. If theoretical S-wave arrives before the end of the P-wave window, then the ending time of the latter is given by $t_s$ −20 s. The T-phase data window starts 40 s before the theoretical arrival time $t_{TP}$ explained previously and finishes 150 s after the arrival of the T phase related to the S wave. Each data window is selected and cut from strong-motion records. After selection, the baseline and instrument response are removed. For each component, the PGAs of P and S waves and T phases, without filtering, are computed. The final PGA amplitude corresponds to the maximum acceleration among the three components.

For the T-phase case, we computed the TPEF as defined by Okal et al. (2003):

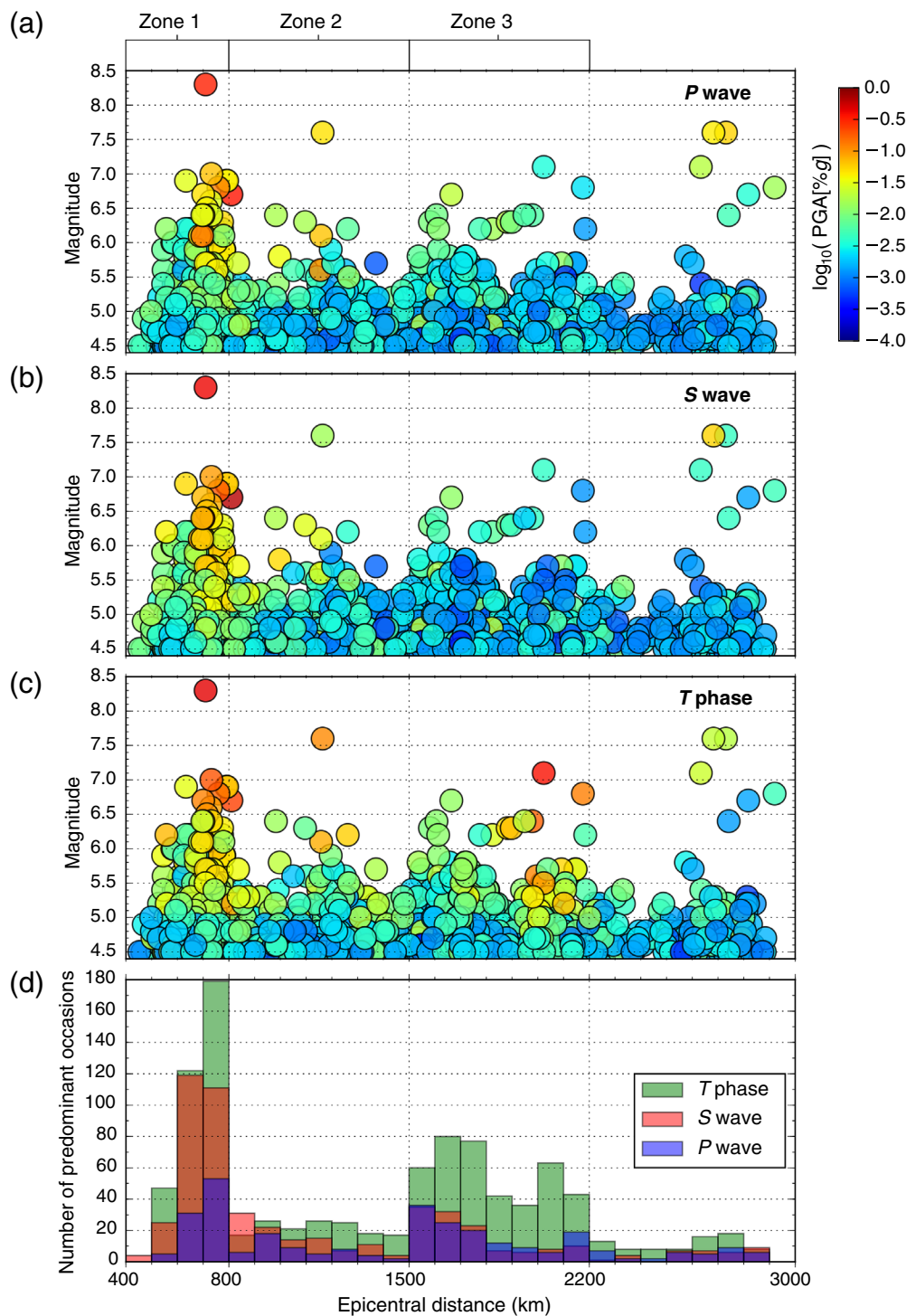$$\text{TPEF} = \rho \alpha \int_W [\dot{u}(t)]^2 \mathrm{d}t, \tag{2}$$

**Figure 2.** Distribution of earthquakes studied in this work as a function of epicentral distance from VA04 station and colored by $\log_{10}$ PGA related to each (a) *P* wave, (b) *S* wave, and (c) *T* phase. (d) Number of occasions when the PGA related to one type of wave is the largest one among the three types, computed in 100 km bins. Zones 1–3 are identified on top. PGA, peak ground acceleration. The color version of this figure is available only in the electronic edition.
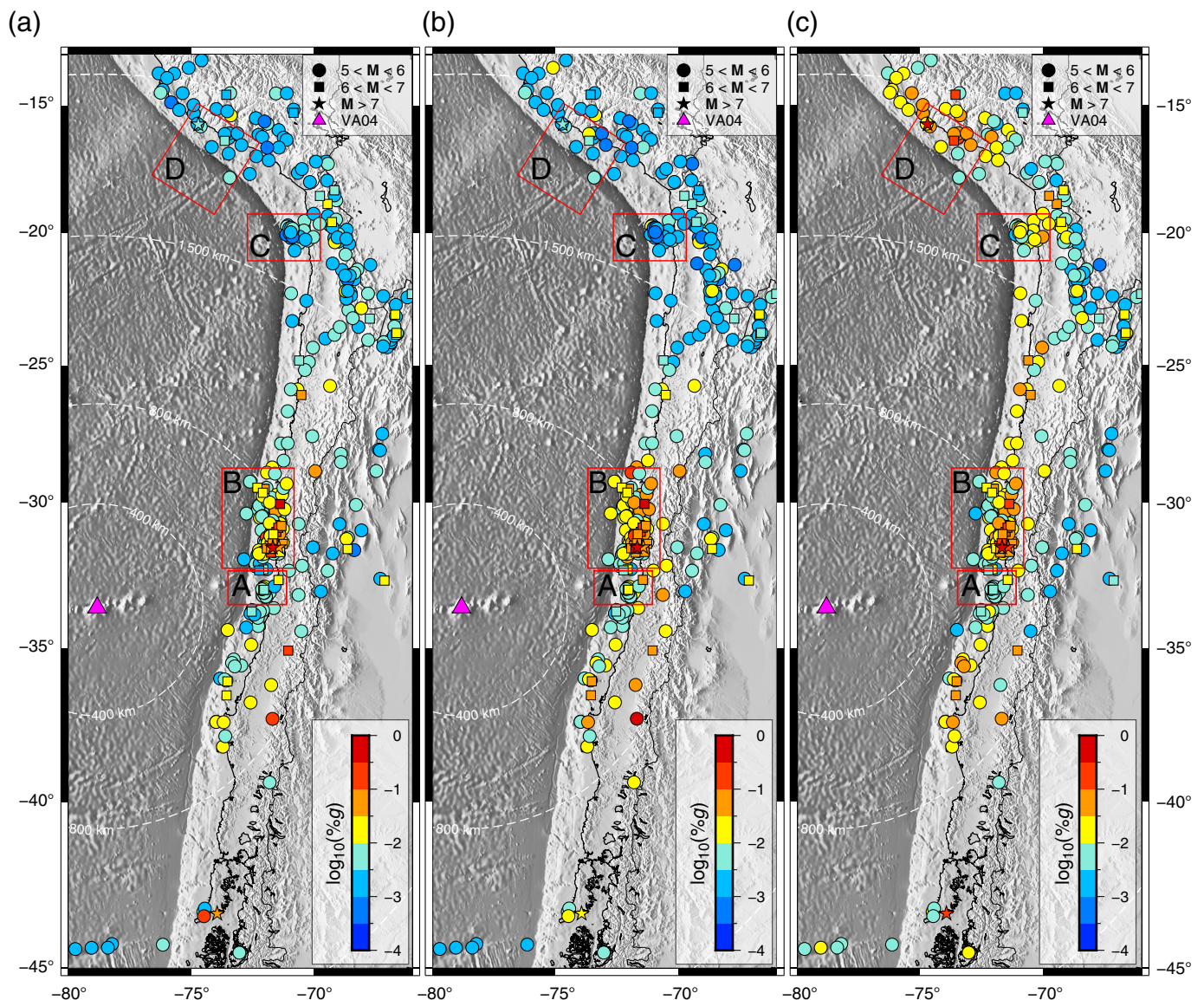
used the same time window obtained for the PGA computation and followed the same approach applied by Sáez and Ruiz (2018). Because we are working with just a single station, our final results are normalized by $\rho$ and $\alpha$.

## Results

### Influence of epicentral distance

Figure 2a–c shows the magnitude of all the earthquakes in our database versus epicentral distance and colored by its PGA amplitude for each *P* and *S* wave and T phase, where we can identify three main groups. We note that major contributions for short distances (zone 1, $\Delta < 800$ km) are mainly from *T* phases and *S* waves, accounting for almost 50% and 34% of the events, respectively. In this sense, the *P* wave is distinctly the minor contributor to the largest PGA in zone 1. In zone 2 (800 km $\leq \Delta <$ 1500 km), its absolute contribution to largest PGA is less than its respective in zone 1, but it is in the same range of predominant occasions than *S* wave, which is even similar to *T*-phase contribution for this zone. A similar behavior is observed in zone 3 (1500 km $\leq \Delta <$ 2200 km), where the absolute contribution of the three type of waves is larger than its respective in zone 2 because there are more earthquakes, but the *P*- and *S*-wave contribution are still in a similar range of predominant occasions. This similar range of *P*- and *S*-wave contribution at zones 2 and 3 can be related to anelastic attenuation of high frequencies

in which $\dot{u}(t)$ is the vertical ground motion, $W$ is the *T*-phase duration, and $\rho$ and $\alpha$ are the density and *P*-wave velocity at the site where the ground motion is measured, respectively. We

along longer travel paths occurred in the upper mantle, where most of the anelastic losses occur in shear deformation (Der, 1998), thus generating low and similar PGA amplitudes for both
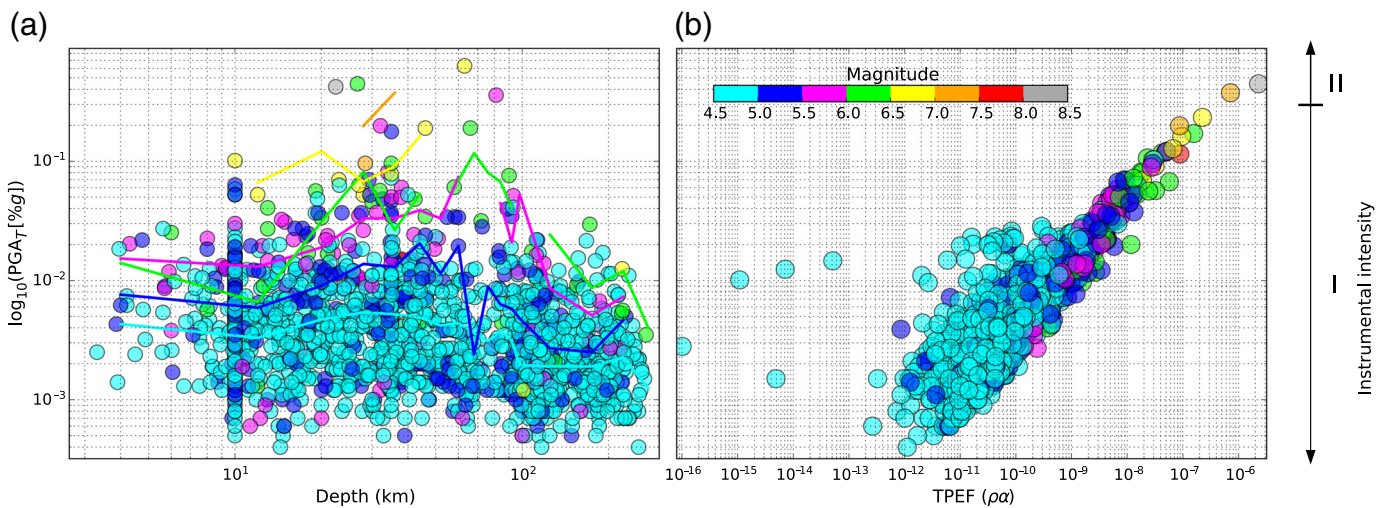
**Figure 3.** PGA amplitudes recorded at VA04 station (magenta triangle). The epicentral location of earthquakes is represented by symbols (square, circle, and star) according to magnitude range (**M** 5–6, **M** 6–7, and **M** > 7, respectively). Seismic sequences related to different large earthquakes are delimited by red boxes: (A) 2017 $M_w$ 6.9 Valparaíso, (B) 2015 $M_w$ 8.3 Illapel, (C) 2014 $M_w$ 8.2 Iquique, and (D) 2018 $M_w$ 7.1 Peru. Color scale is based on the logarithm of each PGA value (percent of gravity acceleration $g$). (a) PGA amplitudes associated with $P$-wave arrival. (b) PGA amplitudes associated with $S$-wave arrival. (c) PGA amplitudes associated with $T$-phase arrival. The same events are plotted on all three panels. White dashed circles denote epicentral distances from VA04 station. The color version of this figure is available only in the electronic edition.

$P$ and $S$ waves. Furthermore, Figure 3 shows the epicentral distribution of the same earthquake catalog as a function of PGA generated by $P$ (Fig. 3a) and $S$ waves (Fig. 3b) and $T$ phases (Fig. 3c), which reveals that PGA amplitudes related to both $S$ and $P$ waves decrease with epicentral distance and do not depend on the event magnitude. However, PGA amplitudes associated with $T$-phase arrivals do not show dependence on epicentral distance, and they are mostly larger than their respective $P$ and $S$ waves (Figs. 2 and 3). This phenomenon can be explained as they mainly travel along the SOFAR channel rather than the upper mantle, where anelastic attenuation does not affect $T$-wave propagation (Thorp, 1965; Okal, 2008).

The PGA zones in Figure 2 can be related to different seismic sequences along the subduction margin. Earthquakes in zone 1 include the 2015 Illapel $M_w$ 8.3 and the 2017 Valparaiso $M_w$ 6.9 seismic sequences (B and A in Fig. 3), and their ground shaking is as large as 0.44%$g$, which is related to the $T$-phase arrival of the 2015 Illapel mainshock. As a whole, sequence A shows lower

amplitudes of PGA at VA04 station than sequence B. Furthermore, zone 2 shows PGA amplitudes up to ~0.1%$g$, where the larger value is associated with the $T$ phase generated by the 2016 $M_w$ 7.6 Chiloé mainshock. This zone also includes

(a)



(b)

**Figure 4.** PGA records at VA04 station related to *T*-wave arrival as a function of (a) hypocentral depth and (b) *T*-phase energy flux (TPEF). Color curves in (a) correspond to the 50th percentile of data along 18 depth bins. Theoretical intensity ranges following Wald *et al.* (1999) are indicated in the right axis. The color version of this figure is available only in the electronic edition.

intraplate intermediate-depth events below the Andean Cordillera (at ~23° S; 68° W) at depths >70 km (as seen in Fig. 1), which show low PGA amplitudes. Finally, events occurring in zone 3 generate larger amplitudes of PGA than those in zone 2. This zone includes earthquakes mostly related to the 2014 Iquique aftershock sequence and to the Peruvian subduction zone, where the largest record is related to the *T* phase generated by the 2018 Las Lomas $M_w$ 7.1 earthquake, which reached amplitudes as large as 0.37%*g*. The rest of the largest PGA amplitudes for this zone are mainly generated by *T* phases from earthquakes occurring in the area surrounding the 2018 $M_w$ 7.1 Las Lomas mainshock (D in Fig. 3).

### *T* phase and PGA values

*T* phases are the main contributors to large PGA amplitudes recorded at station VA04, and we studied the dependence of this variable on hypocentral parameters. We find a slight dependence of strong shaking related to *T* phases on the hypocentral depth of each event. Figure 4a shows an increase in recorded PGA amplitudes for earthquakes triggered at depths between 20 and 50 km, which mostly occur along the plate interface. We use equation (1) to estimate the intensities from PGAs due to arrival of the *T* phase at RCI (Fig. 4). These types of waves could generate detectable shaking on RCI, reaching MMIs of II–III. Indeed, according to intensity reports by ONEMI (Spanish acronym) and their respective association with PGA records during other earthquakes at different sites along the Chilean subduction zone, intensities larger than MMI III have been reported for PGA amplitudes as low as 0.1%*g* (see Table S2); thus, we consider that the *T* phase has the ability to generate ground shaking greater than MMI II.

Furthermore, our computations of TPEF values for each earthquake are in good agreement with its respective PGA reached by *T*-phase arrival, as shown in Figure 4b, where a direct relation between these parameters is evidenced, that is, larger PGA amplitudes are related to larger TPEF values. This observation is not clear when correlating the TPEF values with its respective PGA amplitudes from *P* and *S* waves (see Figs. S3 and S4) due to a higher dispersion of data.

## Discussion

### *T* phases

The largest PGA values are mainly related to *T*-wave arrivals from both near and far events. *P* and *S* waves make strong contributions to ground shaking when earthquakes occur near RCI, but their contributions vanish when the earthquakes occur far from the island, which can be explained by the attenuation of high-frequency of body waves with distance as they propagate through the oceanic lithosphere. Conversely, PGAs related to *T*-wave arrival do not depend on epicentral distance because they can travel long distances through the SOFAR channel without anelastic attenuation (Thorp, 1965; Okal, 2001); thus, high frequencies are preserved along the travel path and emerge at the station location, generating large PGA amplitudes. In particular, the 2018 $M_w$ 7.1 Las Lomas earthquake was recorded at the VA04 station, and its *T* phase generated acceleration and velocity amplitudes larger than *P*- and *S*-wave arrivals, as shown in Figure 5. Moreover, the PGA amplitude of *T*-wave arrival was as large as 0.37%*g* at station VA04 and reached MMIs of II–III on RCI (F. Paredes, personal comm., 2018).

Some features of earthquake generation in subduction-zone processes can be inferred from PGA records of *T*-wave arrivals. The low PGA amplitudes generated by events related to the 2017 Valparaiso earthquake agree well with the respective low *T*-wave energy fluxes due to seamounts on top of the Nazca plate, which act as barriers for *T*-wave propagation (Walker
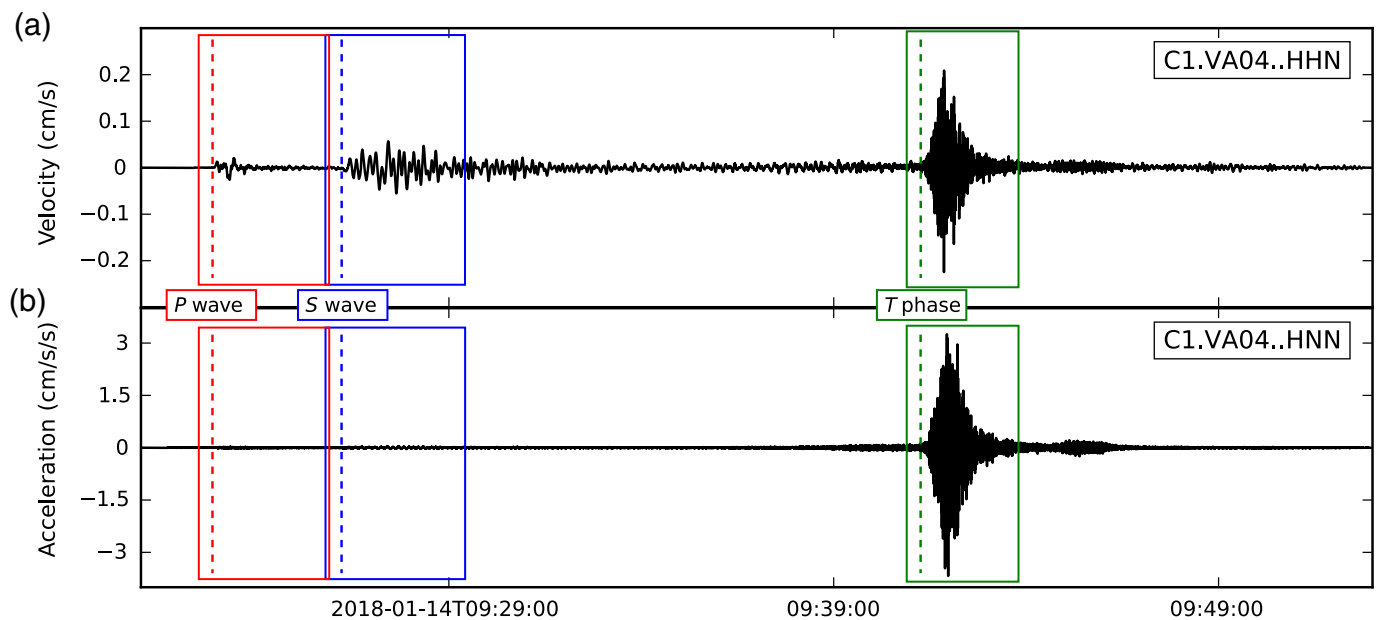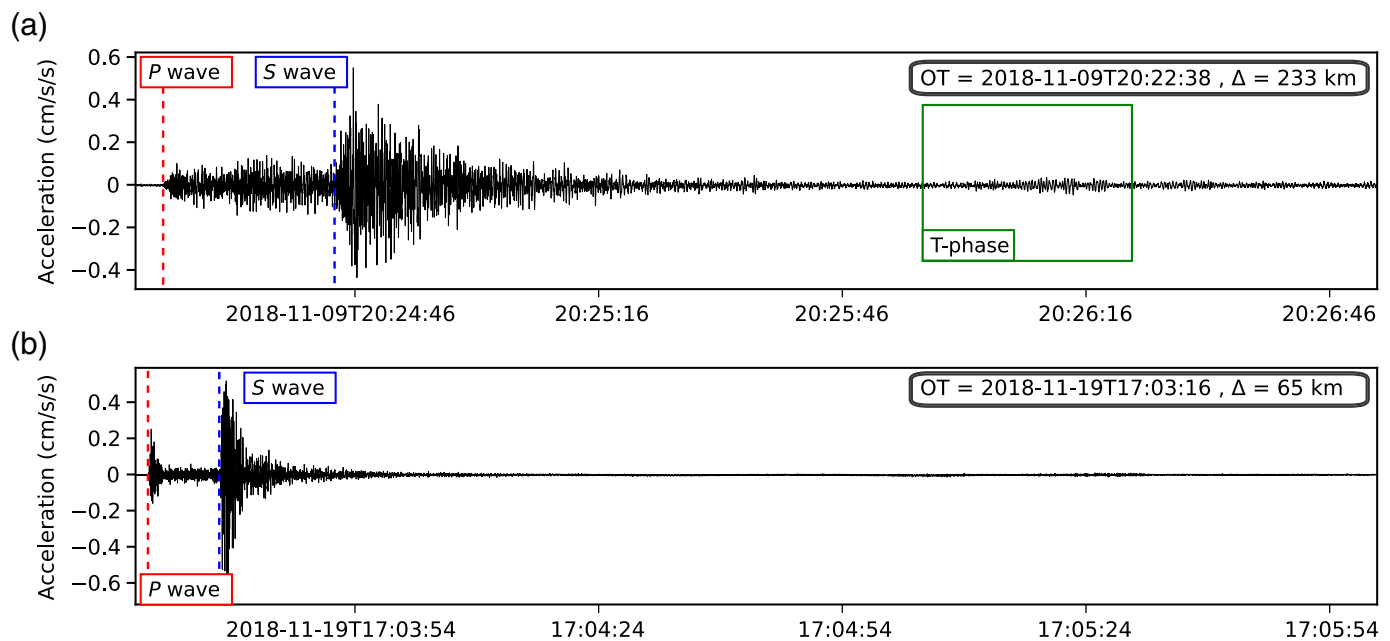
**Figure 5.** Ground-motion records at VA04 station due to the $M_w$ 7.1 Las Lomas earthquake that occurred on 14 January 2018. (a) Nonfiltered ground velocity record from broadband seismometer; (b) nonfiltered ground acceleration record from accelerometer. In both panels, $P$-wave, $S$-wave, and $T$-phase observed arrival times are indicated with red, blue, and green segmented lines, respectively. According to the same color code, the data windows used for computation of each PGA (and TPEF for $T$ phase only) are also indicated. The color version of this figure is available only in the electronic edition.

et al., 1992; Sáez and Ruiz, 2018). However, the aftershock seismicity of the 2015 $M_w$ 8.3 Illapel earthquake, which was distributed along most of the plate interface, shows a dual behavior of PGA generation. In this sense, events occurring below the coastline, where depths between 30 and 45 km are expected, have larger PGA amplitudes than those occurring in the near-trench area for similar magnitude ranges. $T$ waves generated by the latter events travel along similar paths, which do not evidence any topographic barrier for wave propagation reaching the SOFAR channel. This dual behavior can be explained by both a higher attenuation of seismic waves passing through the continental wedge (for shallow near-trench events) and a more effective incidence angle to the SOFAR channel for deeper earthquakes (Sáez and Ruiz, 2018). Nevertheless, it has been proposed that events occurring at deeper depths in the thrust interface have higher stress drop than those ones in the shallower part (e.g., Lay et al., 2012; Yao et al., 2013) meaning that they have an enriched high-frequency content, which would convert into larger PGA amplitudes, but further studies on this topic are required. Thus, a source effect cannot be discarded.

Furthermore, the $T$ phases from the aftershock sequence of the 2014 Iquique earthquake present low PGAs at the VA04 station because these events occurred in the shallower portion of the plate contact zone, mainly between 5 and 25 km depth (León-Ríos et al., 2016), where, although there is no topographic barrier for wave propagation (Fig. S3), the $T$-wave generation is less efficient because of the shallowness of these events. On the other hand, seismicity occurring in the area surrounding the 2018 Las Lomas earthquake (~16° S; 76° W) presents large PGAs for $T$ waves reaching the VA04 station, mainly because these events were located in the deeper part of the plate contact (D in Fig. 3). Some of these PGA values are even larger than the largest PGA value in zone 2 (related to

the $T$ phase of Chiloé 2016 earthquake), which can be explained by differences in the morphology of the continental shelf, leading to different attenuation levels of incident $P$ or $S$ wave entering into the SOFAR channel. The continental shelf in the area of the 2016 Chiloé earthquake is ~60–100 km width (Contreras-Reyes et al., 2010), which is wider than the continental shelf in the area of the 2018 Las Lomas earthquake in the Peruvian subduction zone (<30 km; Contreras-Reyes et al., 2019). Thus, the lower attenuation in the latter area, together with the occurrence of deep events along the thrust interface, could lead to higher PGA values related to $T$-phase propagation in zone 3 rather than zone 2.

These observations have an important influence on ground-shaking assessment in the JFI because they demonstrate that earthquake perception is not always related to tsunami generation. The largest PGA values reached in JFI are usually related to $T$-phase arrival (Fig. 2d), and the TPEF values are in good correlation with PGA related to $T$-phase arrival (Fig. 4b). Then we could indicate that low PGA values can be expected for tsunami earthquakes because they feature strong deficiencies on the TPEF (Okal et al., 2003; Okal, 2008). Tsunami earthquakes are events occurring in the shallow part of the thrust interface, whose rupture process is slower than ordinary subduction-zone

**Figure 6.** Accelerograms (east–west component) of nearby events recorded at VA04 station in RCI. (a) An $m_b$ 4.9 event as reported by the National Seismological Center. (b) Local event located ~65 km southward away from RCI. Observed arrivals for $P$ and $S$ wave and $T$ phase are indicated with red, blue, and green markers, respectively. The color version of this figure is available only in the electronic edition.

thrust earthquakes (Kanamori, 1972; Kanamori and Kikuchi, 1993; Tanioka *et al.*, 1997; Lay *et al.*, 2012), so they have large tsunami potential. Because the tsunami hazard is larger for shallow near-trench earthquakes and the PGA amplitudes related to these events are low, there is a chance that a tsunami earthquake could not be felt in RCI. In contrast, a large megathrust earthquake, breaking at least the B and C domains of the thrust interface, as indicated by Lay *et al.* (2012), can generate large PGA amplitudes on RCI, which would be felt by the population and would likely generate a large tsunami.

### Other potential ground-shaking sources

In addition to feeling earthquakes that occur along the Chilean margin, inhabitants of RCI have reported perceptions of other events. In this sense, ground-shaking perception was reported late in 1998 with MMIs up to III and was related to seismicity generated by volcanic activity near the island (ONEMI, 1999). Recently, according to the CSN catalog (see Data and Resources), an $m_b$ 4.9 tectonic earthquake occurred on 9 November 2018 at 20:22 UTC. Although the epicentral location of this event is hard to constrain because of scarce network coverage, the reported locations from both CSN and NEIC differ by ~30 km distance. Anyway, according to $S$-$P$ time and phase observations on stations located along Chilean coast, we can confirm that this event comes from ~233 km to the west of RCI (Fig. 6a). According to this information, this event could be directly related to seismic activity surrounding the hot spot area (blue circle in Fig. 1) or to the progression of the JFR along the Nazca plate (Lara *et al.*, 2018). Days later, another seismic event was recorded on 19 November 2018 at 17:03 UTC with shorter $S$-$P$ times of ~9 s, ~65 km from station VA04 (Fig. 6b), in the surrounding area of the RCI. Thus, although the JFR is considered an aseismic ridge (Von Huene *et al.*, 1997; Yáñez *et al.*, 2001), these recent

events, together with seismicity recorded in the 1980s and in 1998, provide more evidence about the existence of intraplate seismicity in the surrounding area of the JFI. These events were not felt in RCI. Indeed, the PGA amplitudes were ~0.06%$g$ and were related to the $S$-wave arrival rather than $T$ phase, which is identified for the first event but is practically nonexistent for the second one (Fig. 6). Because the source mechanism and the characteristics of this seismicity are still unclear, it is not possible to confirm or dismiss the existence of any tsunamigenic source. Thus, we suggest that this surrounding area near JFI should be studied more in detail, making use of VA04 station data and one-single station seismic patterns searching techniques.

### Conclusions

We assessed the ground acceleration related to the arrival of $P$ and $S$ waves and $T$ phases from earthquakes along the Peru–Chile subduction zone at station VA04 on RCI. Our results show that the largest ground accelerations on RCI are <0.5%$g$ and related to different types of waves; they generate enough ground shaking to be perceived by RCI inhabitants. The type of wave causing the large acceleration differs depending on the epicentral distance of the earthquake. The largest accelerations generated by earthquakes occurring closest to RCI, such as the 2015 Illapel earthquake, would be related to $S$ waves, whereas the largest accelerations generated by distant events, such as

the 2018 Las Lomas earthquake, would be associated with the arrival of $T$ phases.

$T$ phases with the largest accelerations are related to earthquakes occurring in the deeper part of the thrust interface, where highly efficient $T$-wave generation has been proposed, rather than in the shallower part. Consequently, ground-shaking perception on RCI will not always be related to imminent tsunami arrival because the hypocenter is more likely to occur in the deeper part of the interface, where low tsunami potential is expected. Indeed, tsunami earthquakes, which occur in the near-trench area, would not generate large PGA amplitudes on RCI, and people are more likely not to feel ground shaking but to be affected by the tsunami arrival. Finally, ground-shaking perception could also be generated by a large megathrust earthquake, which would slip along the shallower part of the thrust interface and generate a destructive tsunami such as the 2010 Maule earthquake. We revisited and showed evidence for the existence of surrounding intraplate seismicity near JFI. The source characteristics of this type of seismicity are still unclear, so it is not possible to dismiss the presence of any tsunamigenic source, but further research will be helpful to clarify this point.

## Data and Resources

Seismological data from VA04 station were collected by the National Seismological Center (CSN, www.sismologia.cl, last accessed August 2019) and distributed by Incorporated Research Institutions for Seismology Data Management Center (IRIS-DMC). Waveforms can be reached through IRIS-DMC website at https://ds.iris.edu/ds/nodes/dmc/forms/breqfast-request (last accessed July 2019). The seismicity catalog was retrieved from National Earthquake Information Center–U.S. Geological Survey (NEIC-USGS) database at https://earthquake.usgs.gov/earthquakes/search (last accessed July 2019). Some plots were made using the Generic Mapping Tools v.5.2.1 (Wessel et al., 2013). The supplemental material for this article includes figures and tables showing additional metadata information, $P$- and $S$-wave features, and official reported intensities in Chile for large earthquakes.

## Acknowledgments

## References

Amante, C., and B. W. Eakins (2009). ETOPO1 1 arc-minute global relief model: Procedures, data sources and analysis, NOAA Technical Memorandum NESDIS NGDC-24, National Geophysical Data Center, NOAA, doi: 10.7289/V5C8276M.

Beyreuther, M., R. Barsch, L. Krischer, T. Megies, Y. Behr, and J. Wassermann (2010). ObsPy: A Python toolbox for seismology, Seismol. Res. Lett. 81, no. 3, 530–533.

Carrasco, S., J. A. Ruiz, E. Contreras-Reyes, and F. Ortega-Culaciati (2019). Shallow intraplate seismicity related to the Illapel 2015 Mw 8.4 earthquake: Implications from the seismic source, Tectonophysics 766, 205–218, doi: 10.1016/j.tecto.2019.06.011.

Cesca, S., F. Grigoli, S. Heimann, T. Dahm, M. Kriegerowski, M. Sobiesiak, C. Tassara, and M. Olcay (2016). The $M_w$ 8.1 2014 Iquique, Chile, seismic sequence: A tale of foreshocks and aftershocks, Geophys. J. Int. 204, no. 3, 1766–1780.

Chilean National Emergency Office (ONEMI) (1999). Informe "Misión a Archipiélago Juan Fernández, monitoreo sísmico y gestión de riesgos", available at http://repositoriodigitalonemi.cl/web/bitstream/handle/2012/117/ONE1145.pdf?sequence=1 (last accessed February 2019) (in Spanish).

Contreras-Reyes, E., E. R. Flueh, and I. Grevemeyer (2010). Tectonic control on sediment accretion and subduction off south central Chile: Implications for coseismic rupture processes of the 1960 and 2010 megathrust earthquakes, Tectonics 29, no. 6, doi: 10.1029/2010TC002734.

Contreras-Reyes, E., P. Muñoz-Linford, V. Cortés-Rivas, J. P. Bello-González, J. A. Ruiz, and A. Krabbenhöft (2019). Structure of the collision zone between the Nazca ridge and the Peruvian convergent margin: Geodynamic and seismotectonic implications, Tectonics doi: 10.1029/2019TC005637.

Crotwell, H. P., T. J. Owens, and J. Ritsema (1999). The TauP toolkit: Flexible seismic travel-time and ray-path utilities, Seismol. Res. Lett. 70, no. 2, 154–160.

Cua, G., D. J. Wald, T. I. Allen, D. Garcia, C. B. Worden, M. Gerstenberger, K. Lin, and K. Marano (2010). "Best practices" for using macroseismic intensity and ground motion-intensity conversion equations for hazard and loss models in GEM1 (p. 4), GEM Technical Report 2010-4, GEM Foundation, Pavia, Italy, available at https://cloud-storage.globalquakemodel.org/public/wix-new-website/pdf-collections-wix/publications/GEM-TechnicalReport_2010-4.pdf (last accessed October 2019).

Der, Z. A. (1998). High-Frequency P-and S-Wave Attenuation in the Earth, in Q of the Earth: Global, Regional, and Laboratory Studies, Birkhäuser, Basel, Switzerland, 273–310.

Fritz, H. M., C. M. Petroff, P. A. Catalán, R. Cienfuegos, P. Winckler, N. Kalligeris, R. Weiss, S. E. Barrientos, G. Meneses, C. Valderas-Bermejo, et al. (2011). Field survey of the 27 February 2010 Chile tsunami, Pure Appl. Geophys. 168, no. 11, 1989–2010.

Kanamori, H. (1972). Mechanism of tsunami earthquakes, Phys. Earth Planet. In. 6, 346–359.

Kanamori, H., and M. Kikuchi (1993). The 1992 Nicaragua earthquake: a slow tsunami earthquake associated with subducted sediments, Nature 361, no. 6414, 714.

Kennett, B. L., E. R. Engdahl, and R. Buland (1995). Constraints on seismic velocities in the Earth from traveltimes, Geophys. J. Int. 122, no. 1, 108–124.

Lange, D., J. Ruiz, S. Carrasco, and P. Manríquez (2018). The Chiloé $M_w$ 7.6 earthquake of 2016 December 25 in Southern Chile and its relation to the $M_w$ 9.5 1960 Valdivia earthquake, Geophys. J. Int. 213, no. 1, 210–221.

Lara, L. E., J. Reyes, and J. Diaz-Naveas (2018). $^{40}Ar/^{39}Ar$ constraints on the age progression along the Juan Fernández Ridge, SE Pacific, Front. Earth Sci. 6, 194.

Lay, T., H. C. J. Kanamori, K. D. Ammon, A. R. Koper Hutko, L. Ye, H. Yue, and T. M. Rushing (2012). Depth-varying rupture properties of subduction zone megathrust faults, *J. Geophys. Res.* **117,** no. B04311, doi: 10.1029/2011JB009133.

León-Ríos, S., S. Ruiz, A. Maksymowicz, F. Leyton, A. Fuenzalida, and R. Madariaga (2016). Diversity of the 2014 Iquique's foreshocks and aftershocks: clues about the complex rupture process of a $M_w$ 8.1 earthquake, *J. Seismol.* **20,** no. 4, 1059–1073.

Leyton, F., A. Leopold, G. Hurtado, C. Pastén, S. Ruiz, G. Montalva, and E. Sáez (2018). Geophysical characterization of the Chilean seismological stations: First results, *Seismol. Res. Lett.* **89,** no. 2A, 519–525.

Li, L., T. Lay, K. F. Cheung, and L. Ye (2016). Joint modeling of teleseismic and tsunami wave observations to constrain the 16 September 2015 Illapel, Chile, $M_w$ 8.3 earthquake rupture process, *Geophys. Res. Lett.* **43,** no. 9, 4303–4312.

Melgar, D., W. Fan, S. Riquelme, J. Geng, C. Liang, M. Fuentes, G. Vargas, R. M. Allen, P. Shearer, and E. J. Fielding (2016). Slip segmentation and slow rupture to the trench during the 2015, $M_w$ 8.3 Illapel, Chile earthquake, *Geophys. Res. Lett.* **43,** no. 3, 961–966.

Montessus de Ballore, F. (1911/1916). *Historia Sísmica de los Andes Meridionales, al sur del Paralelo XVI*, Cervantes, Santiago de Chile, Chile (in Spanish).

Okal, E. A. (2001). T-phase stations for the International Monitoring System of the Comprehensive Nuclear-Test Ban Treaty: A global perspective, *Seismol. Res. Lett.* **72,** no. 2, 186–196.

Okal, E. A. (2008). The generation of T waves by earthquakes, *Adv. Geophys.* **49,** 1–65.

Okal, E. A. (2011). *T waves*, in *Encyclopedia of Solid Earth Geophysics*, H. Gupta (Editor), Earth Sciences Series, Springer, Dordrecht, The Netherlands, 1421–1423.

Okal, E. A., P. J. Alasset, O. Hyvernaud, and F. Schindelé (2003). The deficient *T* waves of tsunami earthquakes, *Geophys. J. Int.* **152,** no. 2, 416–432.

Ruiz, S., and R. Madariaga (2018). Historical and recent large megathrust earthquakes in Chile, *Tectonophysics* **733,** 37–56, doi: 10.1016/j.tecto.2018.01.015.

Ruiz, S., F. Aden-Antoniow, J. C. Baez, C. Otarola, B. Potin, F. del Campo, P. Poli, C. Flores, C. Satriano, F. Leyton, *et al.* (2017). Nucleation phase and dynamic inversion of the $M_w$ 6.9 Valparaíso 2017 earthquake in Central Chile, *Geophys. Res. Lett.* **44,** 10,290–10,297, doi: 10.1002/2017GL075675.

Ruiz, S., E. Klein, F. del Campo, E. Rivera, P. Poli, M. Metois, C. Vigny, J. C. Baez, G. Vargas, F. Leyton, R. Madariaga, *et al.* (2016). The seismic sequence of the 16 September 2015 $M_w$ 8.3 Illapel, Chile, earthquake, *Seismol. Res. Lett.* **87,** no. 4, 789–799.

Ruiz, S., M. Moreno, D. Melnick, F. del Campo, P. Poli, J. C. Baez, F. Leyton, and R. Madariaga (2017). Reawakening of large earthquakes in south central Chile: The 2016 $M_w$ 7.6 Chiloé event, *Geophys. Res. Lett.* **44,** 6633–6640, doi: 10.1002/2017GL074133.

Sáez, M., and S. Ruiz (2018). Controls on the T phase energy fluxes recorded on Juan Fernandez Island by continental seismic wave paths and Nazca bathymetry, *Geophys. Res. Lett.* **45,** no. 6, 2610–2617.

Sutcliffe, T. (1839). *The Earthquake of Juan Fernandez, as It Occurred in the Year 1835*, Longman, Orme and Co., London, United Kingdom.

Tanioka, Y., L. J. Ruff, and K. Satake (1997). What controls the lateral variation of large earthquake occurrence along the Japan trench? *Island Arc* **6,** 261–266.

Thorp, W. H. (1965). Deep-ocean sound attenuation in the sub- and low-kilocycle-per-second region, *J. Acoust. Soc. Am.* **38,** no. 4, 648–654.

Tilmann, F., Y. Zhang, M. Moreno, J. Saul, F. Eckelmann, M. Palo, Z. Deng, A. Babeyko, K. Chen, J. C. Baez, *et al.* (2016). The 2015 Illapel earthquake, central Chile: A type case for a characteristic earthquake? *Geophys. Res. Lett.* **43,** no. 2, 574–583.

Udías, A., R. Madariaga, E. Buforn, D. Muñoz, and M. Ros (2012). The large Chilean historical earthquakes of 1647, 1657, 1730, and 1751 from contemporary documents, *Bull. Seismol. Soc. Am.* **102,** no. 4, 1639–1653.

Von Huene, R., J. Corvalán, E. R. Flueh, K. Hinz, J. Korstgard, C. R. Ranero, and W. Weinrebe (1997). Tectonic control of the subducting Juan Fernández Ridge on the Andean margin near Valparaiso, Chile, *Tectonics* **16,** no. 3, 474–488.

Wald, D. J., V. Quitoriano, T. H. Heaton, and H. Kanamori (1999). Relationships between peak ground acceleration, peak ground velocity, and modified Mercalli intensity in California, *Earthq. Spectra* **15,** no. 3, 557–564.

Walker, D. A., C. S. McCreery, and Y. Hiyoshi (1992). T-phase spectra, seismic moments, and tsunamigenesis, *Bull. Seismol. Soc. Am.* **82,** no. 3, 1275–1305.

Wessel, P., W. H. Smith, R. Scharroo, J. Luis, and F. Wobbe (2013). Generic Mapping Tools: Improved version released, *Eos Trans. AGU* **94,** no. 5, 409–410.

Wysession, M. E., E. A. Okal, and K. A. Miller (1991). Intraplate seismicity of the Pacific basin, 1913–1988, *Pure Appl. Geophys.* **135,** 261–359.

Yáñez, G. A., C. R. Ranero, R. von Huene, and J. Díaz (2001). Magnetic anomaly interpretation across the southern central Andes (32°–34° S): The role of the Juan Fernández Ridge in the late Tertiary evolution of the margin, *J. Geophys. Res.* **106,** no. B4, 6325–6345.

Yao, H., P. M. Shearer, and P. Gerstoft (2013). Compressive sensing of frequency-dependent seismic radiation from subduction zone megathrust ruptures, *Proc. Natl. Acad. Sci. Unit. States Am.* **110,** no. 12, 4512–4517.